

# ECHO21: Exploring the Cosmos with Hydrogen Observation

Shikhar Mittal \*

<sup>1</sup>*Battcock Centre for Experimental Astrophysics, Cavendish Laboratory, J. J. Thomson Avenue, Cambridge CB3 0HE, UK*

Accepted —. Received —; in original form —

## ABSTRACT

We introduce a python package called ECHO21 for generating global 21-cm signal from the dark ages through cosmic dawn to the end of reionization. Because of its analytical-prescription-based foundation, ECHO21 generates a single model in  $\mathcal{O}(1)$  s. The code can generate a large set of signals, ideal for building emulators and performing astrophysical or cosmological inference from a given 21-cm dataset. The code is MPI parallel with reasonable scalability and thus, can be run on high-performance computers. We offer six astrophysical parameters that control the Lyman- $\alpha$  emissivity, X-ray emissivity, emissivity of ionizing photons, and star formation rate. A critical component of 21-cm modelling, but ignored by majority of public codes, that we include is the Ly $\alpha$  heating. For a certain range of astrophysical parameters, the Ly $\alpha$  heating could even dominate the X-ray heating. In addition to astrophysical parameters, in ECHO21 it is just as easy to vary the standard cosmological parameters which makes it possible to combine constraints from 21-cm observations and other cosmological probes. Further, we offer two models of star formation rate; a physically-motivated and an empirically-motivated. Since the latter is directly inferred by *HST*/*JWST* observations, it makes ECHO21 an appropriate tool to build synergies between 21-cm observations and galaxy surveys. With a number of 21-cm experiments soon to provide cosmic dawn 21-cm data, ECHO21 is a handy package for making quick but sufficiently realistic astrophysical inferences.

**Key words:** cosmology: theory – dark ages, reionization, first stars – intergalactic medium – software: public release

## 1 INTRODUCTION

Dark ages and the cosmic dawn are not well understood periods of cosmic timeline because of the lack of direct observational probes. One probe that could potentially unravel the physics of the first stars is the hyperfine transition line of wavelength 21 cm originating in a neutral hydrogen atom. The notion of 21-cm line as cosmological probe originated in the 1990s (Madau et al. 1997) and has ever since seen significant improvements in its modelling. See review articles by Furlanetto et al. (2006), Pritchard & Loeb (2012), Barkana (2016) and Mesinger (2019).

Besides its usefulness in understanding the ionization and thermal history, 21-cm line has also been proposed to study primordial magnetic fields (e.g. Bhaumik et al. 2025), gravitational waves (e.g. Mishra & Hirata 2018), fundamental nature of dark matter (e.g. Katz et al. 2024), among others. The wide applicability of 21-cm line as a cosmological probe has lead to the development of many experiments targetting the global 21-cm signal, such as Experiment to Detect the Global EoR Signal (*EDGES*, Bowman et al. 2018), Shaped Antenna measurement of the background RAdio Spectrum (*SARAS*, Singh et al. 2022), and Radio Experiment for the Analysis of Cosmic Hydrogen (*REACH*, de Lera Acedo et al. 2022).

One of the primary goals of the current cosmology is to

analyse and robustly interpret 21-cm signal data from experiments and make inferences about standard or even exotic astrophysical and/or cosmological processes. This has motivated the development of public codes which predict global cosmic dawn 21-cm signal for a wide range and choice of astrophysical parameters. Numerical or semi-numerical codes while accurate and rich in physics, can be slow to run. This necessitates the requirement of analytic and sufficiently realistic models but fast enough for quick and reliable inferences. With this goal in mind, in this work we introduce a python package called ECHO21, which can produce global 21-cm signal in the redshift range  $0 \leq z \leq 1500$  for a given set of astrophysical and cosmological parameters in  $\sim \mathcal{O}(1)$  s.

A secondary goal behind the development of this code is to provide a physically-motivated global 21-cm signal for the *REACH* data analysis pipeline testing. While an empirical Gaussian model (e.g., Mittal et al. 2024a) can be employed for a quick test of the pipeline, a physically-motivated model of the signal will allow us to make realistic astrophysical inferences with 21-cm observational data. Further, while ECHO21 models may be less accurate than semi-numerical models, ECHO21 is easily modified to include new physics.

This paper is organized as follows. In section 2 we go over the modelling details of the global 21-cm signal from the dark ages to the end of epoch of reionization (EoR). In section 3 we present the main outputs of ECHO21. We conclude in section 4.

We adopt a flat- $\Lambda$ CDM cosmology with the following parameters:  $h = 0.674 \pm 0.005$ ,  $\Omega_m = 0.315 \pm 0.007$ ,  $\Omega_b =$

\* E-mail: sm2941@cam.ac.uk

$0.049 \pm 0.001$ ,  $\sigma_8 = 0.811 \pm 0.006$ , and  $n_s = 0.965 \pm 0.004$  (Aghanim et al. 2020). In addition to these we have the CMB temperature today  $T_{\gamma 0} = 2.7255 \pm 0.0006$  K (Fixsen 2009) and the primordial helium abundance  $Y_p = 0.245 \pm 0.004$  (Aver et al. 2015). All values are quoted with 68% confidence limits. We prefix the distance units with a ‘c’ to indicate a comoving length while no prefix to indicate proper physical lengths.

## 2 THEORY AND METHODS

We begin by writing down the observable 21-cm signal, which is the 21-cm brightness temperature measured against the cosmic microwave background (CMB) temperature and is given by (Furlanetto 2006)

$$T_{21} = 27 \bar{x}_{\text{HI}} \left( \frac{1 - Y_p}{0.76} \right) \left( \frac{\Omega_b h^2}{0.023} \right) \sqrt{\frac{0.15}{\Omega_m h^2} \frac{1+z}{10}} \times \left( 1 - \frac{T_r}{T_s} \right) \text{mK}, \quad (1)$$

where  $T_s$  is the spin temperature,  $T_r = T_\gamma$  is CMB temperature,  $z$  is the redshift, and  $x_{\text{HI}} \equiv n_{\text{HI}}/n_{\text{H}}$  is the ratio of number densities of neutral hydrogen (HI) and total hydrogen (H). In standard calculations the background is taken to be the CMB, hence  $T_r = T_\gamma$ , but for an additional radio flux  $T_r$  will contain another term (Fialkov & Barkana 2019; Mirocha & Furlanetto 2019; Mittal & Kulkarni 2022a; Singal et al. 2023). We consider the excess radio term in a future work.

We assume a two-zone model for the intergalactic medium (IGM). In such a scenario the IGM is considered a composition of HI region (sometimes also called the bulk IGM) and the HII region. HII regions refer to the pockets of fully ionized medium around the galaxies because of the ionizing-UV photons possibly emitted by star-forming galaxies (or active galactic nuclei). Everything outside these HII regions is the HI region. If the electron fraction of the HI region is  $x_e$  and the fraction of volume of HII region with respect to the total volume is  $Q$ , then a ‘globally-averaged’ ionized fraction of the Universe can be written as (Mirocha et al. 2013, 2015)

$$\bar{x}_i = Q + (1 - Q)x_e. \quad (2)$$

Accordingly, the globally-averaged neutral hydrogen fraction is  $\bar{x}_{\text{HI}} = 1 - \bar{x}_i$ .

The spin temperature is (Mittal & Kulkarni 2020)

$$T_s^{-1} = \frac{T_\gamma^{-1} + x_k T_k^{-1} + x_{\text{Ly}}(T_k + T_{\text{se}})^{-1}}{1 + x_k + x_{\text{Ly}} T_k (T_k + T_{\text{se}})^{-1}}, \quad (3)$$

where  $T_k$  is the gas temperature,  $T_{\text{se}} \approx 0.4$  K accounts for the spin-exchange correction (Chuzhoy & Shapiro 2006),  $x_k$  is the collisional coupling, and  $x_{\text{Ly}}$  is the Ly $\alpha$  coupling (Wouthuysen 1952; Field 1958).

The collisional coupling is (Mittal et al. 2022)

$$x_k = \frac{T_\star n_{\text{H}}}{T_\gamma A_{10}} [(1 - x_e) \kappa_{\text{HH}} + x_e \kappa_{\text{eH}} + x_e \kappa_{\text{pH}}], \quad (4)$$

where  $T_\star = 0.068$  K,  $A_{10} = 2.85 \times 10^{-15} \text{ s}^{-1}$  is the Einstein coefficient of spontaneous emission for the hyperfine transition,  $n_{\text{H}}$  is the proper hydrogen number density, and  $\kappa_{i\text{H}}$ ’s are the de-excitation rate of hyperfine transition because of collision between  $i$  and HI (Furlanetto & Furlanetto 2006; Furlanetto et al. 2006; Furlanetto & Furlanetto 2007).

The Ly $\alpha$  coupling is

$$x_{\text{Ly}} = S \frac{J_{\text{Ly}}(z)}{5.54 \times 10^{-8} (1+z) \text{ m}^{-2} \text{ s}^{-1} \text{ Hz}^{-1} \text{ sr}^{-1}}, \quad (5)$$

where  $S$  is the scattering correction and  $J_{\text{Ly}}$  is the total Ly $\alpha$  background. For scattering correction we adopt the approximate form by Chuzhoy & Shapiro (2006), so that

$$S \approx e^{-1.69 \zeta^{2/3}}, \quad (6)$$

where

$$\zeta = \frac{4}{3} \sqrt{\frac{a_{\text{V}} \tau \eta^3}{\pi}}. \quad (7)$$

The Voigt parameter, optical depth, and recoil parameter for Ly $\alpha$  line are  $a_{\text{V}}$ ,  $\tau$  and  $\eta$ . For more details see Mittal & Kulkarni (2020) or Mittal et al. (2022).

The Ly $\alpha$  coupling recipe described above is based upon the wing approximation of Ly $\alpha$  radiative transfer. In this approximation the photons are assumed to be far from the resonance – the wings, where the photons have long mean free paths. However, in our previous work (Mittal et al. 2024b), we showed that multiple line core scatterings affect the intensity profile of the Ly $\alpha$  photons causing a reduction in the Ly $\alpha$  coupling. Incorporating such a numerical model into ECHO21, which has an analytical framework, is beyond the scope of this work and thus, we leave it for a future version of ECHO21. See also Reis et al. (2021) and Semelin et al. (2023).

For the construction of Ly $\alpha$  specific intensity,  $J_{\text{Ly}}$ , we follow Mittal & Kulkarni (2020); we assume that the specific intensity tracks the instantaneous star formation rate with the stellar population having a power-law spectral energy distribution (SED). We account for the contribution of higher Lyman-series photons (up to  $n = 23$ ) in the computation of  $J_{\text{Ly}} = J_{\text{Ly}}(z)$  via radiative cascading (Pritchard & Furlanetto 2006). We assume a uniform spectral index between Ly $\alpha$  and Lyman limit lines. Thus, if  $N_{\text{Ly}}$  is the total number of Lyman series photons and the spectral index is  $-s - 1$  then the SED is

$$\phi_{\text{Ly}}(E) \propto f_{\text{Ly}} \frac{N_{\text{Ly}}}{E_\infty} \left( \frac{E}{E_\infty} \right)^{-s-1}, \quad (8)$$

when expressed as number of photons emitted per unit energy range per stellar baryon. The normalization factor for the above is<sup>1</sup>,

$$\frac{s}{(E_\infty/E_\alpha)^s - 1}, \quad (9)$$

where  $E_\infty = 13.6$  eV and  $E_\alpha = 10.2$  eV are the Lyman limit and Ly $\alpha$  energy, respectively. For our fiducial model we have  $N_{\text{Ly}} = 10000$  and  $s = 2.64$ . This is inspired by the Pop-II stellar model (Barkana & Loeb 2005), where we have defined a single ‘average’ power law index for the broken power-law model. In the code we do not consider  $N_{\text{Ly}}$  to be a free parameter but instead allow it to scale by a dimensionless factor  $f_{\text{Ly}}$ . This introduces the first free parameter in our model, fiducial choice for which is 1. The other free parameter associated with Ly $\alpha$  specific intensity is  $s$ .

The global 21-cm signal requires the knowledge of ionization history and ‘spin history’. Spin history in turn is dependent on thermal history and the knowledge of coupling terms.

<sup>1</sup> If  $s = 0$ , then the normalization factor in equation (8) is  $1/\ln(E_\infty/E_\alpha)$ .

Our task then boils down to the computation of  $T_k$ ,  $x_e$ , and  $Q$ , which we discuss next.

## 2.1 Thermal and ionization history

In this section we discuss the differential equations governing the evolution of  $T_k$ ,  $x_e$ , and  $Q$  of our two-zone IGM model.

### Gas kinetic temperature

The equation describing the evolution of  $T_k$  is

$$\frac{dT_k}{dt} = -2HT_k - \frac{T_k}{1 + x_{\text{He}} + x_e} \frac{dx_e}{dt} + \frac{2}{3n_b k_B} \sum q, \quad (10)$$

where  $k_B$  is the Boltzmann constant,  $x_{\text{He}} = Y_p/[4(1 - Y_p)]$  is the ratio of helium to hydrogen number densities,  $n_b$  is the total baryon number density, and  $q$  is the volumetric heating rate. The first term on the right hand side describes the adiabatic cooling, second term corresponds to the change in energy distribution due to changing particle number and last term accounts for all other heating or cooling processes. In this work we consider Compton heating, Ly $\alpha$  heating and X-ray heating.

The Compton heating term is (Seager et al. 2000)

$$q_{\text{Comp}} = 16 \frac{\sigma_T \sigma_S T_\gamma^4}{m_e c^2} n_{\text{H}} x_e k_B (T_\gamma - T_k), \quad (11)$$

where  $\sigma_T$ ,  $\sigma_S$ ,  $m_e$ , and  $c$  are Thomson scattering cross-section, Stephan-Boltzmann constant, mass of electron, and speed of light, respectively.

The volumetric (proper) heating rate due to Ly $\alpha$  photons is (Mittal & Kulkarni 2020)

$$q_{\text{Ly}\alpha} = 4\pi h_P \Delta\nu_D \frac{H}{\lambda_\alpha} (J_{\text{Ly}}^c I_c + J_{\text{Ly}}^i I_i), \quad (12)$$

where  $h_P$ ,  $\Delta\nu_D$ , and  $\lambda_\alpha$  are Planck's constant, Doppler width for Ly $\alpha$  line, and the Ly $\alpha$  wavelength, respectively. The Ly $\alpha$  intensity due to continuum and injected photons is  $J_{\text{Ly}}^c$  and  $J_{\text{Ly}}^i$ , respectively, such that  $J_{\text{Ly}} = J_{\text{Ly}}^c + J_{\text{Ly}}^i$ .  $I_c$  is the normalized area between the undisturbed continuum Ly $\alpha$  intensity and a scattered one. Similarly,  $I_i$  is defined for injected photons. We use the wing approximation for the computation of  $I_c$  and  $I_i$ .

Finally, we also include heating due to X-ray photons. We follow a simple parametric approach to X-ray heating (Furlanetto 2006); we assume that the integrated X-ray emissivity (energy per unit time per unit comoving volume) tracks the instantaneous star formation rate density (just as in the case of Ly $\alpha$  intensity) so that  $\epsilon_X \propto \dot{\rho}_*$ . We calibrate this correlation to local galaxy observations, which indicate that galaxy-integrated X-ray luminosity ( $L_X$ ) scales linearly with star formation rate (SFR) (see, e.g., Mineo et al. 2012). We adopt a recent value based on the *Chandra* observations of 88 nearby galaxies. For the energy range  $\tilde{E}_0 = 0.5$  to  $\tilde{E}_1 = 8$  keV (Lehmer et al. 2024)

$$C_X(\tilde{E}_0, \tilde{E}_1) = \frac{L_X}{\text{SFR}} = 2.45 \times 10^{32} \text{ W } (\text{M}_\odot \text{yr}^{-1})^{-1}. \quad (13)$$

To account for the contribution of low-energy photons (which have higher interaction cross-section) and high-energy photons (which have longer mean free path) we extrapolate  $C_X$  for energies ranging from  $E_0 = 0.2$  to  $E_1 = 30$  keV

(Mirocha & Furlanetto 2019). Assuming a spectral index of  $-w$ , so that  $L_X(E) \propto E^{-w}$ , we get<sup>2</sup>,

$$C_X(E_0, E_1) = C_X(\tilde{E}_0, \tilde{E}_1) \frac{E_1^{1-w} - E_0^{1-w}}{\tilde{E}_1^{1-w} - \tilde{E}_0^{1-w}}. \quad (14)$$

For our fiducial model we set  $w = 1.5$  which gives  $C_X(E_0, E_1) = 4.74 \times 10^{32} \text{ W } (\text{M}_\odot \text{yr}^{-1})^{-1}$ <sup>3</sup>. If a fraction

$$f_{\text{X,h}} = 1 - (1 - x_e^{0.2663})^{1.3163}, \quad (15)$$

of integrated X-ray emissivity results in IGM heating (Shull & van Steenberg 1985) then our final form for the volumetric (comoving) X-ray heating rate is

$$q_X = f_X \cdot f_{\text{X,h}}(x_e) \cdot C_X(E_0, E_1) \cdot \dot{\rho}_*(z), \quad (16)$$

where we have added another free parameter  $f_X$  whose fiducial value is 1.

Note that the  $C_X$  value we adopt is calibrated to low redshifts. At cosmic dawn the stars are metal-poor (Bromm 2013) and large-scale population synthesis simulations have shown that  $C_X$  increases with decreasing metallicity (Fragos et al. 2013). However, since this variation is not very dramatic, these high-redshift uncertainties can be subsumed in the factor  $f_X$ .

### Bulk IGM electron fraction

Having discussed the thermal evolution, we now move to the ionization history of the bulk IGM. The equation governing the bulk IGM electron fraction  $x_e$  is given by the standard recombination equation (Cyr et al. 2024). In addition to the standard photoionization and recombination, we also consider the ionization by the X-ray photons; ionization by the X-ray photons released by star-forming galaxies becomes important after cosmic dawn (Mirabel et al. 2011). Thus, our complete equation governing the bulk IGM electron fraction is given by

$$\frac{dx_e}{dt} = C_P [\beta(1 - x_e)e^{-E_\alpha/(k_B T_\gamma)} - x_e^2 n_{\text{H}} \alpha_B] + \Gamma_X(1 - x_e), \quad (17)$$

where  $C_P$  is the Peebles' factor,  $\beta$  is the photoionization rate, and  $\Gamma_X$  is the ionization due to X-ray photons. We follow Pequignot et al. (1991) for the temperature dependence of case-B recombination coefficient  $\alpha_B$ , with an additional multiplicative correction factor of  $F = 1.14$  to capture the effective-three-level-atom recombination model (Seager et al. 1999).

We evaluate the photoionization rate (also appearing in the Peebles' factor) at the CMB temperature and *not* the gas temperature; recombination coefficient is still computed at the gas temperature (Chluba et al. 2015). This modification in equation (71), Seager et al. (2000) captures the leading order correction in the full physics of the recombination in

<sup>2</sup> If  $w = 1$ , then equation (14) becomes

$$C_X(E_0, E_1) = C_X(\tilde{E}_0, \tilde{E}_1) \frac{\ln(E_1/E_0)}{\ln(\tilde{E}_1/\tilde{E}_0)}.$$

<sup>3</sup> Note that our fiducial  $C_X$  value is  $\sim 0.14$  times the value adopted by Furlanetto (2006) which was based on Grimm et al. (2003) and Gilfanov et al. (2004).

the ambient CMB bath (Ali-Haïmoud & Hirata 2010; Chluba & Thomas 2011).

We estimate the total ionization rate due to X-ray photons as (see App. A)

$$\Gamma_X \simeq \left( \frac{1}{E_w} + \frac{f_{X,\text{ion}}}{E_\infty} \right) \frac{q_X}{f_{X,\text{h}} n_{\text{HI}}}, \quad (18)$$

where<sup>4</sup>

$$E_w = \frac{w + 3.4}{w + 2.4} \left( \frac{E_1^{-w-2.4} - E_0^{-w-2.4}}{E_1^{-w-3.4} - E_0^{-w-3.4}} \right) - E_\infty, \quad (19)$$

and the enhancement factor

$$f_{X,\text{ion}} = 0.3908 \left( 1 - x_e^{0.4092} \right)^{1.7592}. \quad (20)$$

accounts for the secondary ionization (Shull & van Steenberg 1985; Madau & Fragos 2017).

#### Volume-filling factor: modelling reionization

To model reionization we adopt the analytic approach which does a comparison of ionizing photons against the radiative recombinations. Accordingly the reionization equation describing the volume-filling factor ( $Q$ ) of H II region obtained is (Madau et al. 1999)

$$\frac{dQ}{dt} = \frac{\dot{n}_{\text{ion}}}{n_{\text{H}}^0} - A_{\text{He}} n_{\text{H}} \alpha_{\text{B},10^4} C Q, \quad (21)$$

where  $\dot{n}_{\text{ion}}$  is the comoving volume-averaged emission rate of ionizing photons into the IGM, and  $n_{\text{H}}^0$  is the number density of hydrogen today. We assume that the H II region is maintained at a fixed temperature of  $10^4$  K so that  $\alpha_{\text{B},10^4} = 2.94 \times 10^{-19} \text{ m}^3 \text{ s}^{-1}$ . The clumping factor, to correct for the enhanced recombination rate, of ionized hydrogen is (Shull et al. 2012)

$$C(z) = 20.81(1+z)^{-1.1}. \quad (22)$$

We assume that the reionization of H I and He I proceed simultaneously so that these species can be described by a single equation. The factor  $A_{\text{He}} = 1 + x_{\text{He}}$  in the recombination term accounts for the electron contribution from the first ionization of helium. In this work we do not account for its second ionization due to its high ionization energy resulting in a delayed He II reionization (Haardt & Madau 2012). However, we assume an instantaneous He II reionization at  $z = 4$  for the computation of electron-scattering optical depth (see below).

The source of ionizing photons is an ongoing debate (Robertson 2022). It is generally advocated that the galaxies are the main drivers of reionization (e.g. Robertson et al. 2015; Finkelstein 2016; Naidu et al. 2020; Dayal et al. 2020; Yeh et al. 2023; Atek et al. 2024; Dayal et al. 2024). However, the recent *JWST* observations potentially hint towards AGNs-driven reionization (Muñoz et al. 2024; Madau et al. 2024; Asthana et al. 2024).

We assume a galaxy-dominated ionizing emissivity and that the emissivity tracks the instantaneous SFRD, so that

$$\dot{n}_{\text{ion}} = f_{\text{esc}} I_{\text{ion}} \dot{\rho}_*, \quad (23)$$

<sup>4</sup> Just as the case for Lyman series or X-ray SED, one can define an appropriate limit of  $E_w$  for  $w = -3.4$  or  $-2.4$ .

where the ionizing photon yield,  $I_{\text{ion}}$ , is the rate at which ionizing photon are emitted from star-forming galaxies per unit star formation rate and  $f_{\text{esc}}$  is the fraction of ionizing photons that actually escape the galaxies leaking into the IGM.  $f_{\text{esc}}$  becomes our next free parameter whose fiducial value we set to be 0.01. We have chosen this value such that we have a ‘late’ reionization scenario (Kulkarni et al. 2019); our reionization is complete by  $z \approx 5.3$  (see Fig. 2). In general,  $f_{\text{esc}}$  is expected to be a function of halo mass and/or redshift (see, e.g., Dayal et al. 2020; Saldana-Lopez et al. 2023; Lin et al. 2023; Mutch et al. 2023). In the first version of ECHO21 we consider a constant value of  $f_{\text{esc}}$  and leave more general models for a future version.

The ionizing photon yield in general is determined by stellar physics and initial mass function (IMF). For Kroupa IMF and a metallicity of  $0.01 Z_\odot$  (Madau & Fragos 2017),

$$I_{\text{ion}} = 10^{53.44} \text{ s}^{-1} \left( \text{M}_\odot \text{ yr}^{-1} \right)^{-1}. \quad (24)$$

The CMB observations provide a complementary probe to the epoch of reionization. For a given reionization history we compute the electron-scattering optical depth to  $z$  as (Kuhlen & Faucher-Giguère 2012)

$$\tau_e(z) = c \sigma_{\text{T}} n_{\text{H}}^0 \int_0^z [1 + N(z) x_{\text{He}}] Q(z) \frac{(1+z)^2}{H(z)} dz, \quad (25)$$

where  $N(z) = 1 + \Theta(4 - z)$ , for Heaviside step function  $\Theta$ . Function  $N$  accounts for an additional electron contribution from singly ionized helium for  $z \geq 4$  and for two electrons from doubly ionized helium for  $z < 4$ .

We now have three ordinary differential equations, (10), (17), and (21). Note that the two zones, H I and H II regions, evolve independently of each other. As a result, only two of the equations, namely (10) and (17) are coupled, while (21) can be independently solved. We initialize the system at a high redshift  $z = 1500$ , when the gas and CMB temperature are equal, i.e.  $T_{\text{k}} = T_\gamma = 4090.23$  K. For a high-density medium such as at  $z = 1500$  we expect Saha’s equation to be valid (equilibrium version of equation 17). For our fiducial choice of cosmological parameters we get  $x_e = 0.949$ . Note that we activate Ly $\alpha$  heating, X-ray heating and X-ray ionization only after the beginning of star formation, which we choose to begin at  $z = z_*(= 59)$ . Thus, for  $z > z_*$  SFR is 0 and so are  $q_{\text{Ly}}$ ,  $q_{\text{X}}$  and  $\Gamma_{\text{X}}$ . Similarly, reionization has no meaning before cosmic dawn, and thus  $\dot{Q} = 0$  for  $z > z_*$ . Additionally, note that equation (21) is valid only until  $Q$  reaches 1. When  $Q = 1$ , we set  $\dot{Q} = 0$ .

## 2.2 Star formation rate density

In our model we assume that all three emissivities, namely Lyman-series, X-ray, and ionization track the instantaneous SFRD. In this section go over our star formation prescription as it directly controls the IGM heating and ionization. In ECHO21 we consider two types of model for SFRD, namely a physically-motivated model and an empirically-motivated model.

### Physically-motivated model

For our physically-motivated model we estimate the SFRD as the rate at which baryons collapse into the dark matter haloes and convert to star particles with a star formation efficiency (SFE),  $f_*$ . Thus, a physically-motivated (comoving) SFRD is

$$\dot{\rho}_*(z) = \frac{\Omega_b}{\Omega_m} \frac{d}{dt} \int_{M_{h,\min}}^{\infty} f_* M_h \frac{dn}{dM_h} dM_h, \quad (26)$$

where  $M_h$  is the halo mass and  $(dn/dM_h) \cdot dM_h$  is the number density of haloes with masses in the range  $M_h$  to  $M_h + dM_h$ . In general, the SFE is a function of both redshift and halo mass (see, e.g., Fialkov et al. 2013; Mirocha et al. 2016; Park et al. 2019; Mittal & Kulkarni 2022b). In this work we assume only a constant SFE ( $f_* = 0.1$ ) and leave the  $z$ - or  $M_h$ -dependent models for a future work.

Although, Press & Schechter (1974, hereafter press74) is known to under-predict  $dn/dM_h$  for high halo masses (Sheth & Tormen 1999), computations with press74 HMF are faster because it allows to write down a closed form of collapse fraction (Barkana & Loeb 2004). However, as we will see later, the difference in the resulting 21-cm signal is negligible when a more accurate form, such as Tinker et al. (2008) is used. Hence, our fiducial choice for the dark matter HMF,  $dn/dM_h$ , is the press74 form. We obtain HMF using the python package COLOSSUS (Diemer 2018).

The minimum halo mass  $M_{h,\min}$  capable of hosting stars is often parametrized by the minimum virial temperature  $\min(T_{\text{vir}})$ , is (Barkana & Loeb 2004; Dayal & Ferrara 2018)

$$M_{h,\min} = 10^8 \frac{1}{\sqrt{\Omega_m} h^2} M_\odot \left[ \frac{10}{1+z} \frac{0.6}{\mu} \frac{\min(T_{\text{vir}})}{1.98 \times 10^4} \right]^{3/2}. \quad (27)$$

where  $\mu \approx 1.22$ . For the physically-motivated model  $\min(T_{\text{vir}})$  is a free parameter, fiducial choice for which is  $10^4$  K corresponding to an atomic-cooling threshold (Oh & Haiman 2002). Fig. 1 shows SFRD for various HMFs, namely press74 (blue solid), Sheth & Tormen (1999, ‘sheth99’; red-dashed) and Tinker et al. (2008, ‘tinker08’; green-dotted) HMF.

### Empirically-motivated model

Besides the physically-motivated SFRD model described above we also consider an empirical SFRD model. Although, an empirical model has no theoretical backing, it is directly constrained by galaxy surveys data. Further, ECHO21 computations with empirical model of SFRD are faster than even the physically-motivated press74 model by about an order of magnitude.

Based on the luminosity function measurements by Hubble Space Telescope (*HST*) surveys, Madau & Dickinson (2014) proposed an empirical model for the cosmic star formation rate density.<sup>5</sup> Their model explains the low-redshift SFRD quite well. However, it overestimates the SFRD for  $z \gtrsim 8$ ;

<sup>5</sup> Note that the SFRD values inferred (and hence the empirical fit to them) based on the observed luminosity function, are subject to the choice of limiting luminosity or equivalently the magnitude. As shown by Park et al. (2019), choosing a lower limiting luminosity leads to a higher SFRD. In this work we continue with the SFRD fit inferred based on the limiting magnitude adopted by many recent studies (e.g. Donnan et al. 2023, 2024).

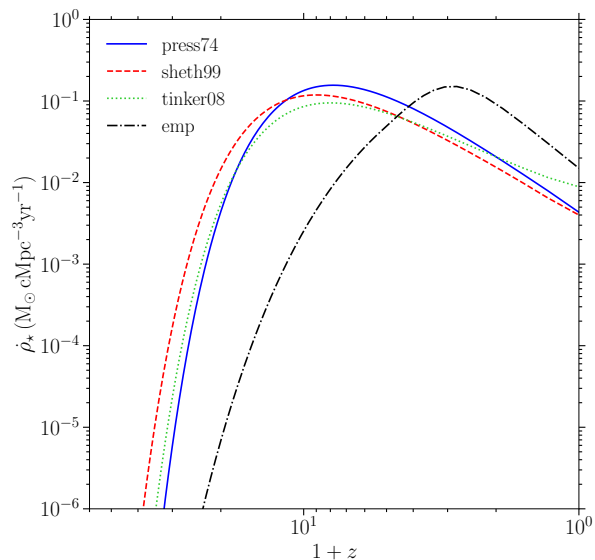


**Figure 1.** Comoving cosmic star formation rate density in the redshift range  $0 \leq z \leq 59$ . For all physically-motivated models (equation 26) we adopt 10% SFE and  $10^4$  K minimum virial temperature. The solid-blue, dashed-red, and dotted-green curves correspond to Press-Schechter (‘press74’), Sheth-Tormen (‘sheth99’), and Tinker (‘tinker08’) HMF, respectively. The dash-dotted-black curve is the empirically-motivated model of SFRD (equation 28).

recent *JWST* observations reveal that SFRD has an exponential drop rather than a power-law drop in the range  $8 \lesssim z \lesssim 13$  (Donnan et al. 2023; Harikane et al. 2023; Donnan et al. 2024). Observations by *HST* in the pre-*JWST* era have also hinted towards this behaviour (e.g., McLeod et al. 2016). Above  $z \sim 13$ , the SFRD trend is much more uncertain because of the lack of spectroscopic confirmation of galaxy candidates observed by *JWST*. Although, there is now a growing evidence towards an even sharper decline in SFRD then an exponential drop above  $z \sim 13$  (e.g. Robertson et al. 2024), further corroboration is needed.

Given the above discussion, we assume a Madau-Dickinson form at low redshifts while an exponential form at high redshifts. Thus, our empirical SFRD is given as

$$\dot{\rho}_*(z) = \begin{cases} \frac{0.015(1+z)^{2.73}}{1 + [(1+z)/3]^{6.24}} & \text{if } 0 \leq z \leq 4, \\ \dot{\rho}_*(z=4) \cdot 10^{-a(z-4)} & \text{if } z > 4. \end{cases} \quad (28)$$

in units of  $M_\odot \text{yr}^{-1} \text{cMpc}^{-3}$ . We consider one free parameter here:  $a$ , which we define as

$$a = - \left. \frac{d \log_{10} \dot{\rho}_*}{dz} \right|_{z>4} \quad (29)$$

fiducial values for which is 0.257 (Gupta et al. 2025). Note that we do not consider any free parameter associated with the low-redshift SFRD as it accurately explains observations in this redshift range. The black dash-dotted curve in Fig. 1 shows the empirically-motivated SFRD with the fiducial value of  $a$ .

Just as in the case of a physically-motivated model, we assume the star formation with the rate density given by equation (28) to begin at  $z = 59$ . Thus, we assume the exponential form continues to be valid at high redshifts.

This completes our discussion of IGM modelling and the required ingredients. Table 1 summarises our free astrophysical parameters and their fiducial values. Note that we do not consider star formation efficiency ( $f_*$ ) to be a free parameter since it is degenerate with  $f_{\text{Ly}}$ ,  $f_X$ , and  $f_{\text{esc}}$ . Similarly, we have the yield of ionizing photons ( $I_{\text{ion}}$ ) as it is degenerate with  $f_{\text{esc}}$ .

### 3 RESULTS AND DISCUSSION

In this section we will look at the results generated by our code ECHO21. In section 3.1 we look at a single realization of the global signal for our fiducial choice of parameters. Here we also show the evolution of electron fraction, volume-filling factor, and gas temperature from dark ages through the epoch of reionization until today. In section 3.2 we investigate the impact of the choice of SFRD model on the global signal. In section 3.3 we explore a large parameter space of astrophysical and cosmological parameters.

#### 3.1 Fiducial model

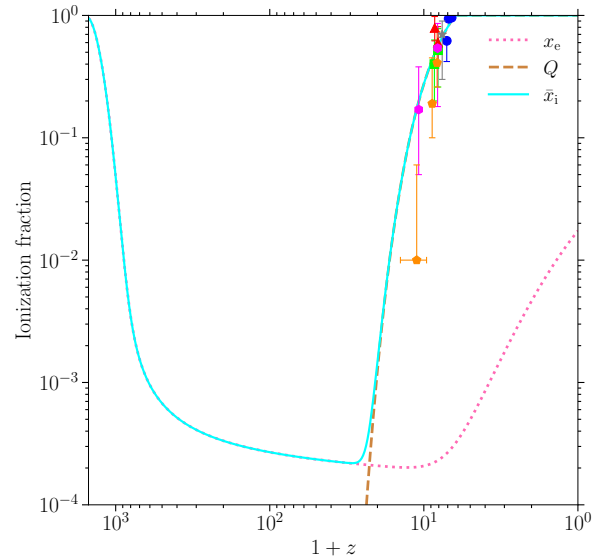
We first show results for our fiducial model. Fig. 2 shows the trend for the bulk IGM electron fraction ( $x_e$ ), volume-filling factor ( $Q$ ) and the two-zone-model-averaged ionization fraction ( $\bar{x}_i$ ) with redshift. The trend for  $x_e$  agrees with the standard recombination calculations (see, e.g., Peebles 1968; Seager et al. 1999, 2000). In the absence of external ionizing sources  $x_e$  would saturate to  $\sim 2 \times 10^{-4}$  by the end of epoch of reionization. However, X-rays emitted in the comic dawn period with their long mean free path can penetrate deep into the IGM and cause ionizations resulting in a rise in  $x_e$ . For fiducial model we see this for  $z \lesssim 9$ .

Fig. 2 also shows the progression of epoch of reionization by the dashed-brown curve. The redshift of reionization (when the Universe was 50% ionized) is  $z_{\text{re}} = 7.42$  (which is within  $1\sigma$  uncertainty bars of *Planck* 2018 results;  $7.64 \pm 0.74$ ) and the redshift when the Universe is fully ionized is  $z = 5.30$ , in agreement with large Ly $\alpha$  opacity fluctuations and low CMB optical depth data (Kulkarni et al. 2019). In the same figure we also show constraints on the reionization from various probes and techniques. These include dark gaps in the Ly $\alpha$  forest (McGreer et al. 2014), quasar damping wings (Greig et al. 2016; Davies et al. 2018; Greig et al. 2019), the effective Ly $\alpha$  opacity of the IGM (Ning et al. 2022), Ly $\alpha$  emission equivalent widths (Nakane et al. 2024), and galaxy damping wings (Umeda et al. 2024). As evident, our fiducial model of reionization (represented by dashed-brown curve) is in reasonable agreement with inferences from various observations.

Finally, relevant to the calculation of 21-cm signal (equation 1) we also show the two-zone-model-averaged ionization fraction,  $\bar{x}_i$ , defined in equation (2).

Another probe of EoR is the electron-scattering optical depth. In Fig. 3 we show the electron-scattering optical depth as a function of  $z$ . For our fiducial model the total optical depth (by setting  $z = z_*$  in equation 25) comes out to be  $\tau_e \approx 0.0592$  which is within  $1\sigma$  uncertainty bars of *Planck* 2018 results;  $0.054 \pm 0.007$ .

Fig. 4 left panel shows the gas, CMB and the spin temperature as a function of redshift and the right panel shows the



**Figure 2.** Bulk IGM electron fraction ( $x_e$ , dotted pink), volume-filling factor ( $Q$ , dashed brown), and two-zone-model-averaged ionization fraction ( $\bar{x}_i$ , solid cyan) computed using ECHO21. In this fiducial model, 50% reionization is complete by 7.42 and 100% by  $z = 5.3$ . We also show constraints on the state of ionization from some of the recent literature, namely McGreer et al. (2014, blue circles), Greig et al. (2016, 2019, red triangles), Davies et al. (2018, green squares), Ning et al. (2022, grey star), Nakane et al. (2024, orange pentagons), and Umeda et al. (2024, magenta hexagons).

corresponding global 21-cm signal, which is the main product of ECHO21. Although, we set our starting of cosmic dawn at  $z = 59$ , gas temperature is seen to rise (for fiducial model, dominantly due to Ly $\alpha$  heating) only after  $z \sim 14.8$  before which it drops adiabatically. Still, the effect of star formation can be seen as early as  $z = 29.3$  when the Ly $\alpha$  photons by the newly formed stars start to render the signal in absorption. At this stage the global signal is  $-4.71$  mK.

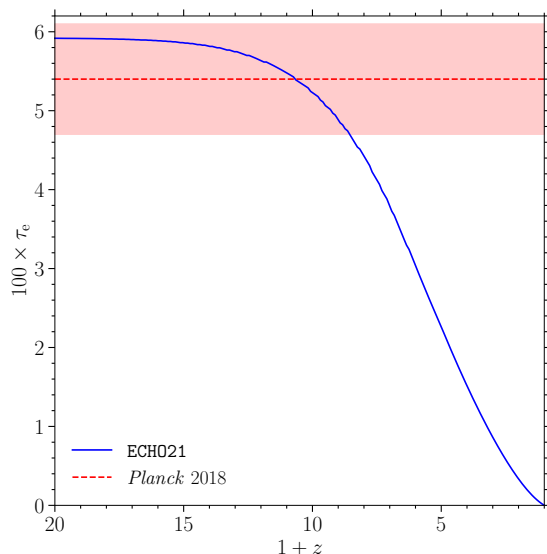
The first absorption peak (in the dark ages) is  $-41.10$  mK observed at  $z = 87.5$ . This absorption is caused by hydrogen-electron and hydrogen-hydrogen collisions. The second absorption peak (in the cosmic dawn) is  $-186.23$  mK observed at  $z = 16.6$ . This absorption is dominantly induced by the Ly $\alpha$  photons. The maximum emission signal (in the epoch of reionization) is  $2.38$  mK at  $z = 6.6$ . Once the Universe becomes completely ionized by  $z = 5.3$ , the signal disappears.

Fig. 5 shows the trends of couplings with redshift. The collisional coupling is high in the dark ages but drops rapidly as the gas temperature and gas density drop with the expanding Universe. However, we see a small rise in  $x_k$  at  $z \approx 14.5$  as a result of rising temperature due to gas heating dominantly by Ly $\alpha$  photons at cosmic dawn. But eventually the effect of rapid Hubble expansion at low redshifts, and hence density dilution, dominates over temperature rise and again  $x_k$  continues to drop. The dashed red curve shows the Ly $\alpha$  coupling which is only relevant in the cosmic dawn period ( $z < z_*$ ). Since  $x_{\text{Ly}}$  tracks the star formation,  $x_{\text{Ly}}$  rises rapidly for  $z \lesssim 6.5$  whereafter it starts to drop because of the drop in star formation rate at  $z \approx 6.5$ . However, throughout  $z < 28$ ,  $x_{\text{Ly}}$  dominates over  $x_k$  by several orders of magnitude.

**Table 1.** Free astrophysical parameters in ECHO21. The first column gives the parameters, second column gives a brief description of the parameter, and the last column gives the fiducial value. In addition to these parameters, the fiducial choice for HMF will be the Press-Schechter form. Due to its degeneracy with  $f_{\text{Ly}}$ ,  $f_{\text{X}}$ , and  $f_{\text{esc}}$  we fix  $f_{\star}$  to 0.1.

Parameter	Description	Fiducial value
$f_{\text{Ly}}$	Normalization of the Ly $\alpha$ background	1
$s$	Spectral index of Lyman series SED <sup>a</sup>	2.64
$f_{\text{X}}$	Normalization of the X-ray background	1
$w$	Spectral index of X-ray SED <sup>a</sup>	1.5
$f_{\text{esc}}$	Escape fraction of ionizing photons	0.01
$\min(T_{\text{vir}})$	Minimum virial temperature of star-forming haloes (For physically-motivated SFRD)	$10^4$ K
$a$	$-\text{d}(\log_{10} \hat{\rho}_{\star})/\text{d}z _{z>4}$ (For empirically-motivated SFRD)	0.257

<sup>a</sup> When the SED is expressed as energy, and not number, emitted in a unit energy range, i.e.,  $\text{SED} \propto E^{-\beta}$ .



**Figure 3.** Electron-scattering optical depth in the redshift range  $0 \leq z \leq 19$  for our fiducial model generated using ECHO21. The optical depth out to the beginning of cosmic dawn comes out to be 0.0592 which is within  $1\sigma$  limits of *Planck* 2018 results.

Fig. 6 shows the trends of Ly $\alpha$  and X-ray heating for our fiducial model. For our fiducial choice of parameters, Ly $\alpha$  heating dominates over X-ray heating for the majority of redshift range. Only for  $z \lesssim 3.5$  X-ray heating begins to dominate over Ly $\alpha$  heating. A noteworthy consequence of this is that the signal strength does not necessarily scale with  $f_{\text{X}}$  (at least for low  $f_{\text{X}}$  values) monotonically as shown in the past work (e.g. Pritchard & Loeb 2010). Models involving lower number of total Lyman series photons (and hence lower  $f_{\text{Ly}}$ ) do not recover the  $f_{\text{X}}$ -scaling behaviour either because then the spin temperature, and hence the 21-cm signal, does not strongly respond to gas temperature changes. This is because, although lowering  $f_{\text{Ly}}$  reduces Ly $\alpha$  heating, it also lowers  $x_{\text{Ly}}$  and hence  $T_{\text{s}}-T_{\text{k}}$  correspondence.

We draw another conclusion from the above discussion. Because the Ly $\alpha$  heating and coupling have opposing impacts on the signal strength, the signal strength does not scale monotonically with  $f_{\text{Ly}}$  either, as described in previous works. This implies that with all other parameters remaining fixed, there

should be an optimum value of  $f_{\text{Ly}}$  to achieve the deepest signal at cosmic dawn.

Finally, we note that while X-ray photons always cause heating of IGM, Ly $\alpha$  photons can produce cooling effect as well. For our choice of parameters this is observed for  $z \lesssim 1.1$ . The continuum Ly $\alpha$  photons always lead to heating but the cooling is brought about by the injected Ly $\alpha$  photons. After  $z \approx 1.1$ , we find that  $J_{\text{Ly}}^c I_c < |J_{\text{Ly}}^i I_i|$  (see equation 12) and thus  $q_{\text{Ly}} < 0$ , i.e., we get a net cooling effect.

Regarding the above discussion, we note that our lower X-ray heating compared to Ly $\alpha$  heating is only a model specific feature (see also the discussion at the end of the section on gas kinetic temperature), but the qualitative response of the 21-cm signal to  $f_{\text{X}}$  and  $f_{\text{Ly}}$  would still be valid. To reiterate, this is a consequence of non-negligible heating by Ly $\alpha$  photons, which several of the past analytical or semi-numerical 21-cm modelling efforts have ignored.

### 3.2 Impact of SFRD modelling on the 21-cm signal

In this section we explore the impact of SFRD modelling on the 21-cm signal. As described in section 3 we consider two types of SFRD models, namely a physically-motivated model and an empirically-motivated model. Physically-motivated model needs a choice of HMF. In Fig. 7 we show representative cases of 21-cm signal corresponding to press74 (fiducial), Sheth & Tormen (1999, ‘sheth99’), and Tinker et al. (2008, ‘tinker08’) HMFs. Since press74 underestimates SFRD (for  $z \gtrsim 11.8$ , for fiducial model parameters), the activation of Ly $\alpha$  coupling is delayed and so is the 21-cm signal compared to other cases of HMFs. Accordingly, the difference between deepest feature in the solid-blue and dashed-red curve is  $\sim 8.7$  mK and a difference of 2.2 on the redshift axis. From these results it is evident that the choice of HMF is important in the modelling of 21-cm signal. Conversely, given some observational data the choice of HMF will impact the astrophysical parameters inferred. See also Greig et al. (2024), who investigate both these aspects in more detail. Our results on the impact of choice of HMF on the 21-cm signal modelling qualitatively agree with Greig et al. (2024).

For all physically-motivated models we use the same set of cosmological and astrophysical parameters; the fiducial set

<sup>7</sup> We use ‘asinh’ scaling of  $y$  axis in python with a linear width of 0.1.

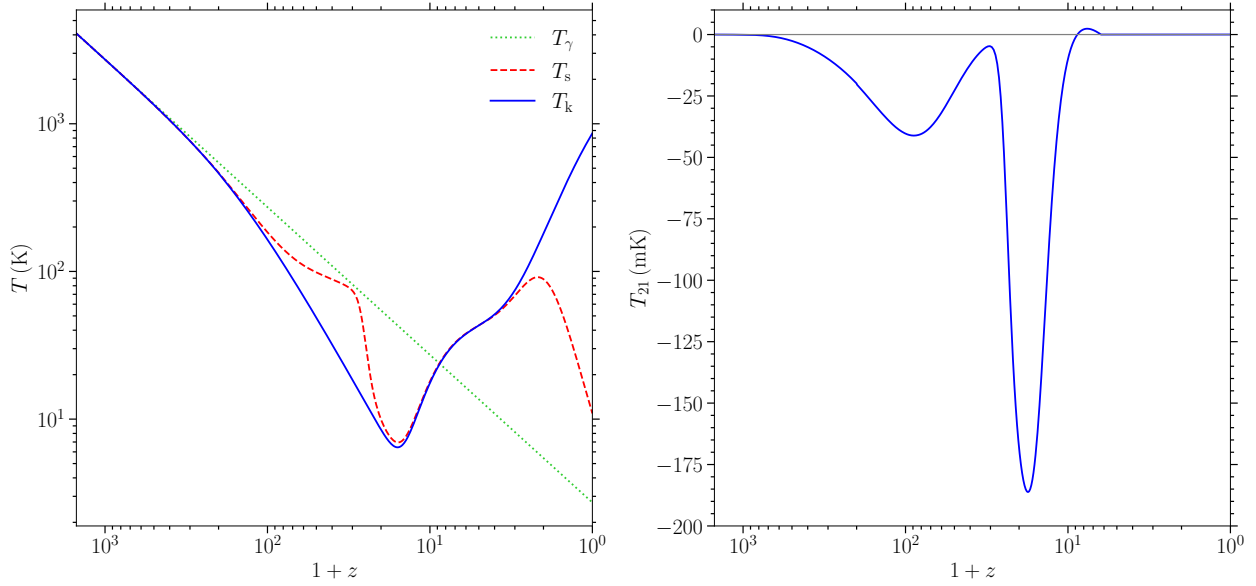


**Figure 4.** Left: gas kinetic temperature (solid blue), CMB temperature (dotted green), and spin temperature (dashed red). Right: the global 21-cm signal. For fiducial set of parameters (see Table 1) the strongest signal is  $-186.23$  mK, observed at  $z = 16.62$ . The redshift range is  $0 \leq z \leq 1500$ , covering dark ages until today.

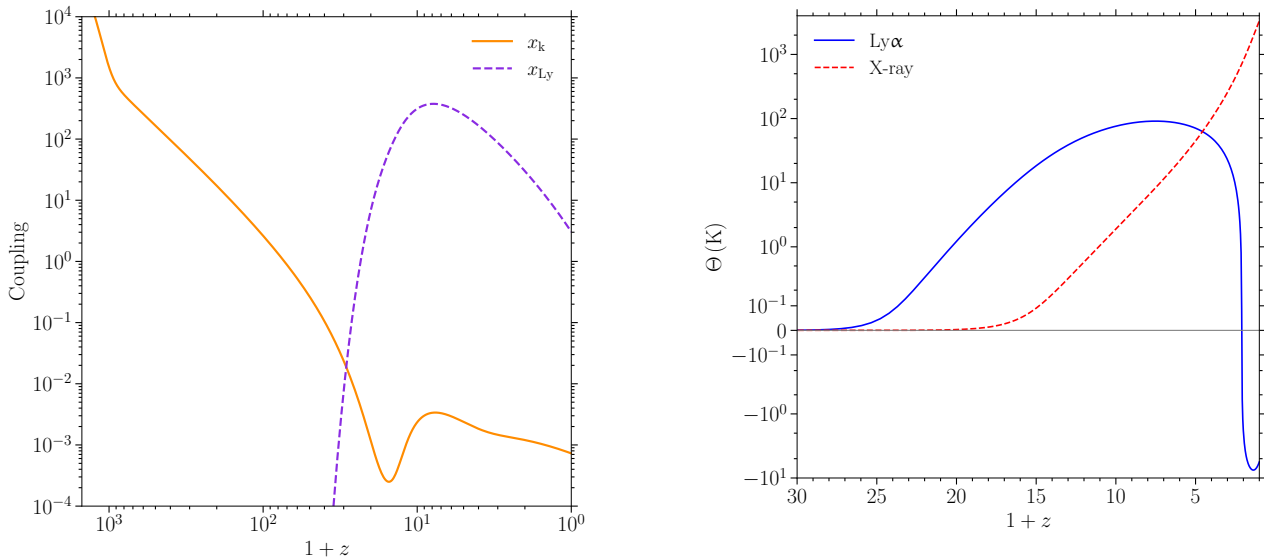


**Figure 5.** Collisional (solid orange) and Ly $\alpha$  (dashed purple) coupling for our fiducial set of parameters. Fig. 4 shows the corresponding spin temperature and 21-cm signal.

**Figure 6.** Comparison of Ly $\alpha$  (solid blue) and X-ray (dashed red) heating in the redshift range  $0 \leq z \leq 29$  for fiducial set of parameters.  $y$  axis<sup>7</sup> shows the quantity  $\Theta = 2q/(3n_b k_B H)$ , which has the units of temperature. X-ray heating remains subdominant to Ly $\alpha$  heating for  $z \gtrsim 3.5$ . Ly $\alpha$  heating is an important term to consider for an accurate modelling of gas temperature evolution.

(see Table 1). Also, note that we used a constant SFE of 10% for all the models. We consider more flexibility in choosing SFE in subsequent versions of ECHO21.

In addition to the physically-motivated models for SFRD we also show 21-cm signal using an empirically-motivated model for SFRD (equation 28). Because of the late kick in of star formation for empirically-motivated SFRD (see dash-

dotted-black curve in Fig. 1), the signal is significantly delayed with respect to the physically-motivated models. The deepest feature in dash-dotted-black curve is shallower by  $\sim 5.4$  mK and shifted by 8.3 on redshift axis compared to solid-blue curve. As mentioned previously, the motivation for considering an empirically-motivated SFRD model is that



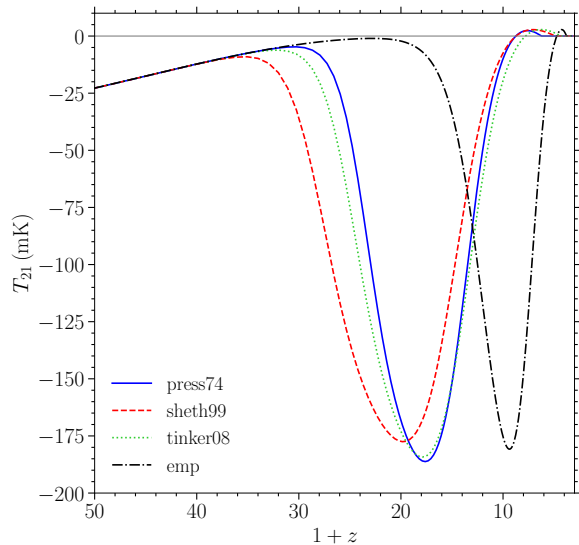


**Figure 7.** Impact of SFRD on the 21-cm signal. Solid-blue curve (repeated from Fig. 4) corresponds to a Press & Schechter (1974) HMF (‘press74’), dashed-red curve corresponds to a Sheth & Tormen (1999) HMF (‘sheth99’), dotted-green curve corresponds to a Tinker et al. (2008) HMF (‘tinker08’), and dash-dotted-black curve corresponds to an empirical SFRD model (equation 28). Fig. 1 shows the SFRD for these models.

such a model is directly constrained by galaxy survey observations allowing for synergies between galaxy surveys and 21-cm observations. Further, computations are much faster compared to those for physically-motivated SFRD model.

### 3.3 Exploring a large parameter space

In section 3.1 we showed a single instance of global signal for fiducial set of parameters. Here we generate global signals for a large number of astrophysical parameters. We choose five equispaced points for all six astrophysical parameters (for physically-motivated model of SFRD) listed in Table 1 so that we have a total of 15625 models. The range is  $[10^{-2}, 10^2]$ ,  $[0, 3]$ ,  $[10^{-1}, 10^3]$ ,  $[0, 3]$ ,  $[0.005, 0.5]$ , and  $[10^2, 10^6]$  K for  $f_{\text{Ly}}$ ,  $s$ ,  $f_{\text{X}}$ ,  $w$ ,  $f_{\text{esc}}$ , and  $\min(T_{\text{vir}})$ , respectively. We consider  $f_{\text{Ly}}$ ,  $f_{\text{X}}$ ,  $f_{\text{esc}}$  and  $\min(T_{\text{vir}})$  to be log-spaced and  $s$  and  $w$  to be linearly spaced. On 10 CPUs, 15625 are generated in approximately 1 hour 22 minutes.

Fig. 8 shows 15625 global signals (magenta-coloured curves) generated using ECHO21 for a large astrophysical parameter space. The cosmological parameters are fixed at their median values mentioned in the introductory section. The solid blue curve shows the fiducial curve repeated from Fig. 4. Note that we show the signals only in the cosmic dawn and EoR range ( $0 \leq z \leq 59$ ) as the astrophysical processes do not impact the dark ages signal. Thus, in this case the dark ages signal is common for all the models.

We find that the signal responds most strongly to parameters  $f_{\text{Ly}}$ ,  $f_{\text{esc}}$  and  $\min(T_{\text{vir}})$ , mildly to  $f_{\text{X}}$  and negligibly to  $s$  and  $w$ . Parameter  $f_{\text{Ly}}$  changes the signal timing and depth, higher  $f_{\text{esc}}$  leads to an earlier disappearance of the signal,  $f_{\text{X}}$  primarily affects the signal depth, and  $\min(T_{\text{vir}})$  primarily affects the signal timing.

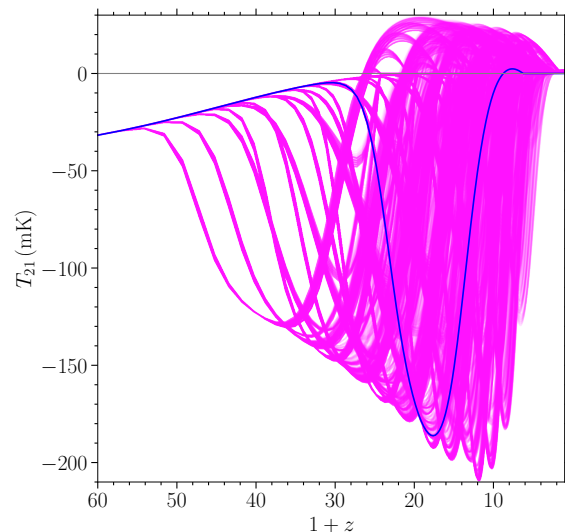


**Figure 8.** 15625 global signals (in magenta) generated with ECHO21 for different astrophysical parameters; we vary  $f_{\text{Ly}}$ ,  $s$ ,  $f_{\text{X}}$ ,  $w$ ,  $f_{\text{esc}}$ , and  $\min(T_{\text{vir}})$ . See text for the range of values we choose. The cosmological parameters are fixed at the mean values quoted at the end of introductory section. The solid blue curve shows the fiducial signal (repeated from Fig. 4).

In ECHO21 it is also possible to vary cosmological parameters just as easily. Similar to Fig. 8, where we showed signals for different astrophysical parameters, in Fig. 9 we show the signals for different cosmological parameters, namely the Hubble parameter ( $H_0$ ), relative total matter density ( $\Omega_{\text{m}}$ ), relative baryon density ( $\Omega_{\text{b}}$ ), amplitude of density fluctuations ( $\sigma_8$ ), spectral index of the primordial scalar spectrum ( $n_s$ ), CMB temperature today ( $T_{\gamma,0}$ ), and primordial helium fraction ( $Y_{\text{P}}$ ). We choose the range of parameters to be that set by the uncertainties (see the introduction section) with a total of three values for each parameter. Thus, if a parameter  $p$  is  $x \pm \epsilon$  then parameter values we explore are  $\{x - \epsilon, x, x + \epsilon\}$ . As a result, we have a total of  $3^7 = 2187$  models. We run these models on 10 CPUs and found to complete in  $\approx 10$  min.

Because the cosmological parameters are so precisely determined (except for  $H_0$ ), the impact of uncertainties in cosmological parameters on the 21-cm signal are rarely investigated. As evident from Fig. 9 the variation in the signal (corresponding to the uncertainties in *Planck*/*WMAP* data) around the fiducial signal model is small. Still, for the chosen uncertainties the strongest signal is  $-198.95$  mK (stronger by 12.72 mK than the fiducial model) observed at  $z \approx 16.2$  while the weakest one is  $-173.80$  mK (weaker by 9.43 mK than the fiducial model) observed at  $z \approx 17$  in the cosmic dawn. In the dark ages, the strongest signal is  $-44.40$  mK and the weakest is  $-37.93$  mK both at  $z \approx 88$ .

Because of the experimental challenges associated with ground-based 21-cm experiments, there are prospects of setting up space- or Moon-based 21-cm experiments, e.g., *DARE* (Burns et al. 2012) and *PRATUSH* (Rao et al. 2023). Space-based 21-cm experiments can potentially dig deeper into the Universe providing a window beyond the cosmic dawn (Koopmans et al. 2021; Fialkov et al. 2024). Physics of the dark ages is expected to be much simpler making dark ages a clean

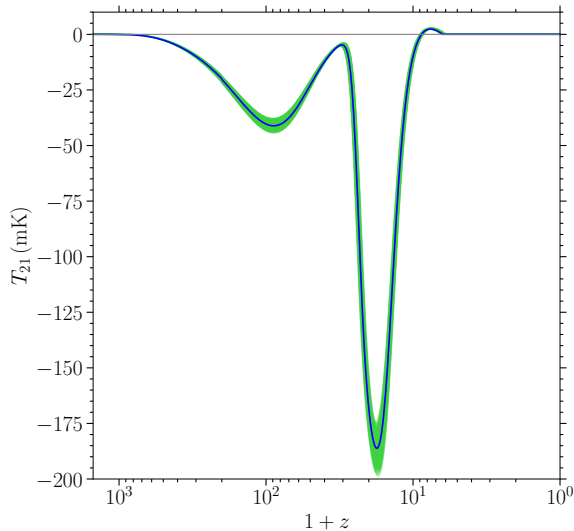


**Figure 9.** 2187 global signals (in green) generated with ECHO21 for different cosmological parameters; we vary  $H_0$ ,  $\Omega_m$ ,  $\Omega_b$ ,  $\sigma_8$ ,  $n_s$ ,  $T_{\gamma 0}$ , and  $Y_P$ . See introductory section for the range of values we choose. The astrophysical parameters are fixed at their fiducial values. The solid blue curve shows the fiducial signal (repeated from Fig. 4).

testing ground for cosmological models. Since ECHO21 allows one to explore the dark ages 21-cm signal for a space of cosmological parameters, it makes ECHO21 an ideal tool to build synergies between 21-cm observations and other cosmological probes of the very early Universe such as BBN predictions, CMB anisotropies, polarization, or lensing (Aghanim et al. 2020). Relatedly, ECHO21 can be used to synergise 21-cm cosmology with the well-known problem of Hubble tension; local distance-ladder measurements lead to a higher measurement of Hubble parameter ( $H_0 = 74.03 \pm 1.42 \text{ kms}^{-1} \text{ Mpc}^{-1}$ ) which are in tension with the value inferred by *Planck* collaboration by  $\sim 5\sigma$  (Riess et al. 2019; Abdalla et al. 2022).

## 4 CONCLUSIONS

In this work we introduced a python package called ECHO21. The basic working behind ECHO21 is to simultaneously solve the differential equations governing the evolution of electron fraction and gas temperature since before the epoch of recombination until the present day accounting for the major processes that impact the histories. These include the standard recombination and photoionization terms throughout the timeline for the ionization history. Once the star formation begins at cosmic dawn (which we choose to be at  $z = 59$ ) we include the ionization due to X-ray photons. For the thermal history, we account for the adiabatic cooling and Compton heating throughout the cosmic timeline. With the star formation in progress, we also account for X-ray heating and Ly $\alpha$  heating. The latter is critical in building an accurate 21-cm signal at cosmic dawn but has been ignored by most public codes.

The main features of the code are as follows:

- 1) For a single set of astrophysical and cosmological pa-

rameters, the code outputs the CMB temperature, gas temperature, spin temperature, electron fraction, and the 21-cm signal throughout the dark ages, cosmic dawn, epoch of reionization until today. Further, it also outputs the volume-filling factor for the cosmic dawn period. For the Press & Schechter (1974) choice of halo mass function (HMF), the total runtime is  $\sim \mathcal{O}(1)$  s.

- 2) In case of multiple parameters, the code outputs the corresponding global signals. As the code is MPI parallel, and because of its reasonable scalability, thousands of models can be generated in a few minutes provided an appropriate choice of high-performance computing resources.

- 3) Current choice of astrophysical parameters include the parameter to scale the number of Lyman series photons, power-law index of Lyman series spectral energy distribution (SED), parameter to scale X-ray luminosity, power-law index of X-ray SED, escape fraction of ionizing photons from galaxies, and a parameter which controls the star formation rate density (SFRD).

- 4) The code offers two choices of SFRD model, namely an empirically-motivated model and a physically-motivated model (default). Further, for the physically-motivated model, one has the option of choosing HMF such as Press-Schechter, Sheth-Tormen, Tinker, etc.

- 5) In addition to exploring 21-cm signals for a wide range of astrophysical parameters, ECHO21 can be used to explore 21-cm signals for a wide range of cosmological parameters. These include  $H_0$ ,  $\Omega_m$ ,  $\Omega_b$ ,  $\sigma_8$ ,  $n_s$ ,  $T_{\gamma 0}$ , and  $Y_P$  where the symbols have the usual meaning.

The first version of ECHO21 is based on a simple but sufficiently realistic model of the intergalactic medium. The simplicity allows for a fast evaluation of global signal from the dark ages to the end of epoch of reionization. The current version of ECHO21 is appropriate for making inferences and deriving constraints on astrophysical or cosmological parameters. It can be used to build synergies between 21-cm observations and probes of cosmological parameters or galaxy surveys. ECHO21 is a developing code and future versions will see further improvements in it.

## ACKNOWLEDGEMENTS

I thank Shikhar Asthana, Jiten Dhandha, Anastasia Fialkov, Girish Kulkarni, Jordan Mirocha, and Sandro Tacchella for comments. It is also a pleasure to acknowledge discussions with several other members of the REACH (Radio Experiment for the Analysis of Cosmic Hydrogen) Collaboration. This work is supported by the ERC (UKRI guaranteed) research grant EP/Y02916X/1.

## DATA AVAILABILITY

We release our a python package called ECHO21, available from PyPI and GitHub (<https://github.com/shikharmittal04/echo21.git>).

## REFERENCES

Abdalla E., et al., 2022, *J. High Energy Astrophys.*, 34, 49

- Aghanim N., et al., 2020, *A&A*, 641, A6
- Ali-Haïmoud Y., Hirata C. M., 2010, *Phys. Rev. D*, 82, 063521
- Asthana S., Haehnelt M. G., Kulkarni G., Bolton J. S., Gaikwad P., Keating L. C., Puchwein E., 2024 ([arXiv:2409.15453](https://arxiv.org/abs/2409.15453))
- Atek H., et al., 2024, *Nature*, 626, 975
- Aver E., Olive K. A., Skillman E. D., 2015, *J. Cosmology Astropart. Phys.*, 2015, 011
- Barkana R., 2016, *Phys. Rep.*, 645, 1
- Barkana R., Loeb A., 2004, *ApJ*, 609, 474
- Barkana R., Loeb A., 2005, *ApJ*, 626, 1
- Bhaumik A., Paul D., Pal S., 2025, *J. Cosmology Astropart. Phys.*, 2025, 089
- Bowman J. D., Rogers A. E. E., Monsalve R. A., Mozdzen T. J., Mahesh N., 2018, *Nature*, 555, 67
- Bromm V., 2013, *Rep. Prog. Phys.*, 76, 112901
- Burns J. O., et al., 2012, *Adv. Space Res.*, 49, 433
- Chluba J., Thomas R. M., 2011, *MNRAS*, 412, 748
- Chluba J., Paoletti D., Finelli F., Rubiño-Martín J. A., 2015, *MNRAS*, 451, 2244
- Chuzhoy L., Shapiro P. R., 2006, *ApJ*, 651, 1
- Cyr B., Acharya S. K., Chluba J., 2024, *MNRAS*, 534, 738
- Davies F. B., et al., 2018, *ApJ*, 864, 142
- Dayal P., Ferrara A., 2018, *Phys. Rep.*, 780-782, 1
- Dayal P., et al., 2020, *MNRAS*, 495, 3065
- Dayal P., et al., 2024 ([arXiv:2401.11242](https://arxiv.org/abs/2401.11242))
- Diemer B., 2018, *ApJS*, 239, 35
- Donnan C. T., et al., 2023, *MNRAS*, 518, 6011
- Donnan C. T., et al., 2024, *MNRAS*, 533, 3222
- Fialkov A., Barkana R., 2019, *MNRAS*, 486, 1763
- Fialkov A., Barkana R., Visbal E., Tseliakhovich D., Hirata C. M., 2013, *MNRAS*, 432, 2909
- Fialkov A., Gessey-Jones T., Dhandha J., 2024, *Philos. Trans. R. Soc. A*, 382, 20230068
- Field G. B., 1958, *Proc. IRE*, 46, 240
- Finkelstein S. L., 2016, *Publ. Astron. Soc. Australia*, 33, e037
- Fixsen D. J., 2009, *ApJ*, 707, 916
- Fragos T., Lehmer B. D., Naoz S., Zezas A., Basu-Zych A., 2013, *ApJ*, 776, L31
- Furlanetto S. R., 2006, *MNRAS*, 371, 867
- Furlanetto S. R., Furlanetto M. R., 2006, *MNRAS*, 374, 547
- Furlanetto S. R., Furlanetto M. R., 2007, *MNRAS*, 379, 130
- Furlanetto S. R., Peng Oh S., Briggs F. H., 2006, *Phys. Rep.*, 433, 181
- Gilfanov M., Grimm H.-J., Sunyaev R., 2004, *MNRAS*, 347, L57
- Greig B., Mesinger A., Haiman Z., Simcoe R. A., 2016, *MNRAS*, 466, 4239
- Greig B., Mesinger A., Bañados E., 2019, *MNRAS*, 484, 5094
- Greig B., Prelogović D., Mirocha J., Qin Y., Ting Y.-S., Mesinger A., 2024, *MNRAS*, 533, 2502
- Grimm H.-J., Gilfanov M., Sunyaev R., 2003, *MNRAS*, 339, 793
- Gupta O., Beniamini P., Kumar P., Finkelstein S. L., 2025 ([arXiv:2501.09810](https://arxiv.org/abs/2501.09810))
- Haardt F., Madau P., 2012, *ApJ*, 746, 125
- Harikane Y., et al., 2023, *ApJS*, 265, 5
- Katz O. Z., Outmezguine N., Redigolo D., Volansky T., 2024, *Nucl. Phys. B*, 1003, 116502
- Koopmans L. V. E., et al., 2021, *Exp. Astron.*, 51, 1641
- Kuhlen M., Faucher-Giguère C.-A., 2012, *MNRAS*, 423, 862
- Kuhlen M., Madau P., 2005, *MNRAS*, 363, 1069
- Kulkarni G., Keating L. C., Haehnelt M. G., Bosman S. E. I., Puchwein E., Chardin J., Aubert D., 2019, *MNRAS*, 485, L24
- Lehmer B. D., et al., 2024, *ApJ*, 977, 189
- Lin Y.-H., et al., 2023, *MNRAS*, 527, 4173
- Madau P., Dickinson M., 2014, *ARA&A*, 52, 415
- Madau P., Fragos T., 2017, *ApJ*, 840, 39
- Madau P., Meiksin A., Rees M. J., 1997, *ApJ*, 475, 429
- Madau P., Haardt F., Rees M. J., 1999, *ApJ*, 514, 648
- Madau P., Giallongo E., Grazian A., Haardt F., 2024, *ApJ*, 971, 75
- McGreer I. D., Mesinger A., D’Odorico V., 2014, *MNRAS*, 447, 499
- McLeod D. J., McLure R. J., Dunlop J. S., 2016, *MNRAS*, 459, 3812
- Mesinger A., ed. 2019, *The Cosmic 21-cm Revolution*. IOP Publishing, [doi:10.1088/2514-3433/ab4a73](https://doi.org/10.1088/2514-3433/ab4a73)
- Mesinger A., Furlanetto S., Cen R., 2011, *MNRAS*, 411, 955
- Mesinger A., Ferrara A., Spiegel D. S., 2013, *MNRAS*, 431, 621
- Mineo S., Gilfanov M., Sunyaev R., 2012, *MNRAS*, 419, 2095
- Mirabel I. F., Dijkstra M., Laurent P., Loeb A., Pritchard J. R., 2011, *A&A*, 528, A149
- Mirocha J., Furlanetto S. R., 2019, *MNRAS*, 483, 1980
- Mirocha J., Harker G. J. A., Burns J. O., 2013, *ApJ*, 777, 118
- Mirocha J., Harker G. J. A., Burns J. O., 2015, *ApJ*, 813, 11
- Mirocha J., Furlanetto S. R., Sun G., 2016, *MNRAS*, 464, 1365
- Mishra A., Hirata C. M., 2018, *Phys. Rev. D*, 97, 103522
- Mittal S., Kulkarni G., 2020, *MNRAS*, 503, 4264
- Mittal S., Kulkarni G., 2022a, *MNRAS*, 510, 4992
- Mittal S., Kulkarni G., 2022b, *MNRAS*, 515, 2901
- Mittal S., Ray A., Kulkarni G., Dasgupta B., 2022, *J. Cosmology Astropart. Phys.*, 2022, 030
- Mittal S., Kulkarni G., Anstey D., de Lera Acedo E., 2024a, *MNRAS*, 534, 1317
- Mittal S., Kulkarni G., Garel T., 2024b, *MNRAS*, 535, 1979
- Muñoz J. B., Mirocha J., Chisholm J., Furlanetto S. R., Mason C., 2024, *MNRAS*, 535, L37
- Mutch S. J., Greig B., Qin Y., Poole G. B., Wyithe J. S. B., 2023, *MNRAS*, 527, 7924
- Naidu R. P., Tacchella S., Mason C. A., Bose S., Oesch P. A., Conroy C., 2020, *ApJ*, 892, 109
- Nakane M., et al., 2024, *ApJ*, 967, 28
- Ning Y., Jiang L., Zheng Z.-Y., Wu J., 2022, *ApJ*, 926, 230
- Oh S. P., Haiman Z., 2002, *ApJ*, 569, 558
- Park J., Mesinger A., Greig B., Gillet N., 2019, *MNRAS*, 484, 933
- Peebles P. J. E., 1968, *ApJ*, 153, 1
- Pequignot D., Petitjean P., Boisson C., 1991, *A&A*, 251, 680
- Press W. H., Schechter P., 1974, *ApJ*, 187, 425
- Pritchard J. R., Furlanetto S. R., 2006, *MNRAS*, 367, 1057
- Pritchard J. R., Loeb A., 2010, *Phys. Rev. D*, 82, 023006
- Pritchard J. R., Loeb A., 2012, *Rep. Prog. Phys.*, 75, 086901
- Rao M. S., et al., 2023, *Exper. Astron.*, 56, 741
- Reis I., Fialkov A., Barkana R., 2021, *MNRAS*, 506, 5479
- Riess A. G., Casertano S., Yuan W., Macri L. M., Scolnic D., 2019, *ApJ*, 876, 85
- Robertson B. E., 2022, *ARA&A*, 60, 121
- Robertson B. E., Ellis R. S., Furlanetto S. R., Dunlop J. S., 2015, *ApJ*, 802, L19
- Robertson B., et al., 2024, *ApJ*, 970, 31
- Saldana-Lopez A., et al., 2023, *MNRAS*, 522, 6295
- Seager S., Sasselov D. D., Scott D., 1999, *ApJ*, 523, L1
- Seager S., Sasselov D. D., Scott D., 2000, *ApJS*, 128, 407
- Semelin B., et al., 2023, *A&A*, 672, A162
- Sheth R. K., Tormen G., 1999, *MNRAS*, 308, 119
- Shull J. M., van Steenberg M. E., 1985, *ApJ*, 298, 268
- Shull J. M., Harness A., Trenti M., Smith B. D., 2012, *ApJ*, 747, 100
- Singal J., et al., 2023, *PASP*, 135, 036001
- Singh S., et al., 2022, *Nat. Astron.*, 6, 607
- Tinker J., Kravtsov A. V., Klypin A., Abazajian K., Warren M., Yepes G., Gottlöber S., Holz D. E., 2008, *ApJ*, 688, 709
- Umeda H., Ouchi M., Nakajima K., Harikane Y., Ono Y., Xu Y., Isobe Y., Zhang Y., 2024, *ApJ*, 971, 124
- Verner D. A., Ferland G. J., Korista K. T., Yakovlev D. G., 1996, *ApJ*, 465, 487
- Wouthuysen S. A., 1952, *AJ*, 57, 31
- Yeh J. Y.-C., et al., 2023, *MNRAS*, 520, 2757

## APPENDIX A: IONIZATION BY X-RAY PHOTONS

Computation of heating and ionization by the X-ray photons is expensive and slow to evaluate because of the multiple integrals involved (Mesinger et al. 2011, 2013; Mittal et al. 2022). As a result we need approximate empirical estimates which are quick to evaluate. This is often the case for X-ray heating (Furlanetto 2006; Mirocha et al. 2015), as we have used in this work (equation 16). However, a similar strategy for ionization rate ( $\Gamma_X$ ) has not been discussed in literature. We devise the following algorithm for a fast evaluation of  $\Gamma_X$ .

In physically-motivated approach, the standard X-ray heating is expressed as (Madau & Fragos 2017)

$$H_X = 4\pi \int_{E_0}^{E_1} (E - E_\infty) \sigma(E) J_X(E, z) dE, \quad (\text{A1})$$

in units of energy per unit time per neutral hydrogen atom. Similarly, the standard ionization (primary – directly by the X-ray photons) rate is

$$\Gamma_X^p = 4\pi \int_{E_0}^{E_1} \sigma(E) J_X(E, z) dE, \quad (\text{A2})$$

where  $E_\infty = 13.6 \text{ eV}$  is the ionization energy of hydrogen,  $\sigma = \sigma(E)$  is the photoionization cross-section of H I–X-ray interaction, and  $J_X = J_X(E, z)$  is the specific intensity (in terms of number of photons) of X-rays. The energy range of X-ray photons effective in heating and ionization of IGM is  $E_0 < E < E_1$ . In this work we take  $E_0$  and  $E_1$  to be 0.2 and 30 keV, respectively.

In our chosen energy range the cross-section can be well-approximated by a power law, i.e.,  $\sigma \sim E^u$ , where  $u = -3.4$  (Verner et al. 1996). Similarly, if the SED (in terms of number) of X-ray photons emitted from star-forming galaxies is a power law of the form  $\phi_X \sim E^v$ , where  $v = -w - 1$ , then at any redshift specific intensity can be approximated to follow the same trend, so that  $J_X \sim E^v$ . Thus, the ratio of heating and primary ionization rate is

$$\frac{H_X}{\Gamma_X^p} = \frac{\int_{E_0}^{E_1} (E - E_\infty) E^{u+v} dE}{\int_{E_0}^{E_1} E^{u+v} dE}. \quad (\text{A3})$$

The above gives

$$E_w \equiv \frac{H_X}{\Gamma_X^p} = \left( \frac{u+v+1}{u+v+2} \right) \left( \frac{E_1^{u+v+2} - E_0^{u+v+2}}{E_1^{u+v+1} - E_0^{u+v+1}} \right) - E_\infty. \quad (\text{A4})$$

Inserting the values of  $u$  and  $v$  in the above we get  $E_w$  as defined in equation (19). Note that the ionization rate  $\Gamma_X^p$  is enhanced by the secondary ionizations. These are enabled by the energetic electrons knocked out from neutral hydrogen by high-energy X-ray photons emitted from star-forming galaxies. The secondary ionization rate can be approximated as  $f_{X,\text{ion}} H_X / E_\infty$ . Accordingly, the total ionization rate is (Kuhlen & Madau 2005)

$$\Gamma_X \simeq \Gamma_X^p + \frac{f_{X,\text{ion}} H_X}{E_\infty}. \quad (\text{A5})$$

Putting together equation (A4) and (A5) we get

$$\Gamma_X \simeq \left( \frac{1}{E_w} + \frac{f_{X,\text{ion}}}{E_\infty} \right) \frac{q_X}{f_{X,h} n_{\text{H I}}}, \quad (\text{A6})$$

where  $q_X = f_{X,h} n_{\text{H I}} H_X$  is the effective volumetric heating rate, for which we already have an empirical formalism (see equation 16). Thus, having computed  $q_X$  it is trivial to obtain  $\Gamma_X$  via equation (A6).

This paper has been typeset from a  $\text{\TeX}/\text{\LaTeX}$  file prepared by the author.